Applied Acoustics 242 (2026) 111079

Contents lists available at ScienceDirect

Applied Acoustics

journal homepage: www.elsevier.com/locate/apacoust

Prediction of diffuser noise footprint of a ducted wind turbine

Rui Pedro Gonçalves [a,b,*], Feroz Ahmed [c], Christophe Schram [a]

[a] von Karman Institute for Fluid Dynamics, 72 chaussée de Waterloo, St-Genesius-Rode, 1640, Belgium
[b] University of Twente, PO Box 217, Enschede, 7500 AE, the Netherlands
[c] Department of Aerospace Engineering, University of Bristol, Queens Building, Bristol, BS8 1TR, United Kingdom

HIGHLIGHTS

- Proposed and validated broadband noise prediction methods for isolated ducts and ducted turbines.
- Isolated duct impingement noise prediction and directivity.
- Diffuser wind turbine noise prediction and directivity.

ARTICLE INFO

Keywords:
Diffuser-augmented wind turbine
Diffuser
Duct
Rotor
Aeroacoustics
Low-fidelity noise prediction
Amiet's theory
Thin annulus
Leading-edge noise
Trailing-edge noise

ABSTRACT

The aerodynamic broadband noise generated by ducted configurations, such as ducted wind turbines or propellers, is of research interest due to its implications for noise pollution. Accurate prediction methods for such configurations remain unavailable for low-fidelity approaches. This paper applies the thin annulus and segmentation models, an Amiet's theory based analytical framework for predicting broadband noise from hollow cylinders, to two ducted configurations. The segmentation approach is further extended to account for the angle of attack in duct geometries. First, the thin annulus model is validated using an isolated duct, showing good agreement between predictions and experimental data. Then, the models are applied to predict the broadband trailing-edge noise of a diffuser-augmented wind turbine. The results highlight the dominance of the diffuser trailing-edge noise in this configuration and demonstrate the improved prediction accuracy of the segmentation model due to its ability to account for the angle of attack. This study provides a comprehensive framework for broadband noise prediction of ducted turbine applications, using inputs derived from RANS simulations, and demonstrates how low-fidelity approaches can be effectively utilized to address the noise prediction of a ducted turbine.

1. Introduction

A diffuser-augmented wind turbine (DAWT) is a wind energy system that integrates a conventional wind turbine with a diffuser-shaped duct to enhance power generation. By incorporating a diffuser or duct, DAWTs alter both the aerodynamic and aeroacoustic characteristics of the system. The airfoil-shaped diffuser, typically positioned at an angle of attack, induces a pressure difference on the suction side, which increases flow velocity across the rotor plane [1–3]. As a result, this effect enhances energy harvesting potential, making it an ideal solution for urban environments due to its compact design and ability to perform well under the unpredictable flow conditions typical of urban settings. However, the aerodynamic advantages of these systems introduce new noise generation mechanisms, as shown in Fig. 1, with the dominant noise sources originating from both the rotor and diffuser. The diffuser creates new noise sources, including broadband noise from the diffuser trailing-edge (TE), modifying the total noise footprint [4]. Furthermore, the increased flow velocity through the rotor plane enhances both the broadband and tonal noise originating from the rotor. Additionally, the tonal noise directivity is modified by the scattering effect of the diffuser [1,4]. In the event of flow with incoming turbulence, leading-edge (LE) broadband noise may also be prevalent in both diffuser and rotor.

While attention in noise prediction methods focuses primarily on the rotor noise, as indicated by Ref. [4], the diffuser can play a dominant role in certain directions and frequencies of the noise spectrum. Previous attempts to predict the diffuser TE noise have used high-fidelity methods [4]; however, there is a gap in using lower-fidelity approaches to predict the noise from isolated ducts and ducted turbine configurations. In our

---

* Corresponding author at: von Karman Institute for Fluid Dynamics, 72 chaussée de Waterloo, St-Genesius-Rode, 1640, Belgium.
Email address: r.goncalves@utwente.nl (R.P. Gonçalves).

https://doi.org/10.1016/j.apacoust.2025.111079
Received 25 March 2025; Received in revised form 24 July 2025; Accepted 11 September 2025

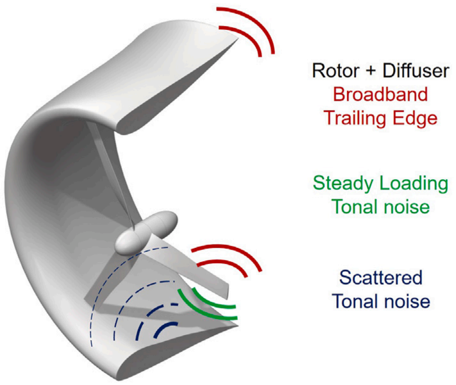

Fig. 1. Conceptual illustration of the dominant noise generation mechanisms in a diffuser-augmented wind turbine. Main noise sources include tonal noise from the rotor, broadband noise from both the leading-edge and trailing-edge of the rotor blades, and trailing-edge broadband noise from the diffuser.

selected approach of using methods with lower computational cost, such as Reynolds-Averaged Navier-Stokes (RANS) and Amiet's theory for the aerodynamic and broadband noise modeling respectively, there is currently no proposed method to address this problem comprehensively. These lower-fidelity methods are simplified yet effective, making them essential for accelerating noise predictions in wind energy systems while maintaining reasonable accuracy.

The thin annulus model for aerodynamic noise was originally outlined by Ref. [5] [5] for leading-edge noise, adapting Amiet's flat plate theory to a circular geometry. In a subsequent study, this model was extended to trailing-edge noise by Ref. [6] [6]. Additionally, [6] [6] proposed an alternative segmentation method that can be effective for duct designs with an angle of attack (AoA). These two models were developed for potential configurations such as ducted wind turbines [1], ducted propulsors [7], isolated ducts [8], ducted fans [8] or ducted propellers [9]. However, both models have so far only been validated using an idealised ring geometry and have yet to be tested on practical engineering configurations.

In our previous study [1], we developed an efficient methodology to predict the aerodynamic noise of a ducted rotor using either three-dimensional simulations or vortex-panel methods informed by two-dimensional strip approaches. Building on that work, the present study proposes two methodologies to predict LE and TE broadband noise from hollow cylindrical structures under axial flow, such as a ducts or diffusers. These predictions are based on the thin annulus and segmentation models, with aerodynamic inputs derived from RANS simulations. The paper is organised as follows: Section 2 describes the numerical methodologies used in the present study, divided into aerodynamic and aeroacoustic components. The results are grouped into aerodynamics or aeroacoustics related, and include validation with an isolated duct (Section 3.1) and predictions for the DAWT (Section 3.2). Finally, Section 4 provides the main conclusions of the study.

2. Methods

This section outlines the hybrid methodology developed to predict broadband aerodynamic noise from ducted configurations, with a specific focus on diffuser-augmented wind turbines (DAWTs). A summary of the simulation workflow, highlighting the prediction of leading-edge (LE) and trailing-edge (TE) noise components, is illustrated in Fig. 2.

The approach combines steady Reynolds-Averaged Navier-Stokes (RANS) simulations with analytical acoustic models derived from Amiet's theory. The aerodynamic component provides boundary layer and turbulence parameters over duct and diffuser surfaces, which serve as inputs for two semi-analytical noise models: the thin annulus and segmentation methods. These models, adapted for hollow cylindrical structures under axial flow, are used to compute LE and TE broadband noise, respectively.

The methodology is validated using three test cases: an isolated cylindrical duct, a full DAWT configuration, and an empty diffuser without a rotor. These cases differ by the presence or absence of the rotor, which influences the aerodynamic modeling approach. For the duct and empty diffuser, two-dimensional axisymmetric simulations are used, while the DAWT employs a three-dimensional sector simulation to capture rotor-induced flow modifications. The thin annulus model, which is well-suited to cylindrical geometries, is applied to both the duct and empty diffuser cases. To account for the angle of attack in the DAWT configuration, the segmentation model is used exclusively for that case.

The following subsections detail the aerodynamic modelling (Section 2.2) and the acoustic prediction methods (Section 2.1).

2.1. *Aeroacoustic source model*

The aeroacoustic sources considered in this work are broadband LE and TE noise, which originate from two primary mechanisms: the interaction of turbulent inflow with the leading edge of the duct or diffuser, and the interaction of the turbulent boundary layer with the trailing edge. Two methods were used to model these noise mechanisms: the thin annulus model, suitable for circular geometries, and the flat plate segmentation approach, which enables angular discretisation and directional flexibility, as described in [6].

Both methods are based on Amiet's theory but differ in how they treat the source geometry. The thin annulus model integrates Amiet's formulation over a cylindrical surface, yielding an exact analytical solution for noise radiated by a symmetric annular structure (see Fig. 3a). In contrast, the flat plate segmentation approach approximates the annular surface by dividing it into discrete flat plate segments, each treated as a separate airfoil (see Fig. 3(b)). Although the thin annulus model offers an exact solution, the segmentation approach is advantageous when introducing an angle of attack in the plates, as explored later.

2.1.1. *Thin annulus*

The thin annulus model [5,6], also referred to as the ring model, allows to compute the acoustic pressure power spectral density (PSD) generated by a ring source located at $\mathbf{y} = (y_1, r_0\Theta)$, where y_1 is the streamwise coordinate, r_0 is the radius and c is the chord length. The acoustic PSD, denoted by $S_{pp}(\mathbf{x}, \omega)$, is calculated at a given angular frequency ω and observer position $\mathbf{x} = (x_1, x_2, x_3)$ in the global cylindrical basis $\mathbf{e} = (e_1, e_2, e_3)$, using the following expressions for the leading- and trailing-edge noise components:

$$S_{pp}^{LE}(\mathbf{x}, \omega) = \left(\frac{\omega \rho c}{4\, c_0 S_0^2} \right)^2 2\pi r_0 U \sum_{n=-\infty}^{\infty} \Phi_{ww}(K_1, k_n) \left| \mathcal{L}^{LE}(x_1, K_1, k_n) \right|^2 |\mathcal{J}|^2 \tag{1}$$

$$S_{pp}^{TE}(\mathbf{x}, \omega) = \left(\frac{\omega c}{4\, c_0 S_0^2} \right)^2 \frac{\pi r_0}{2 U_c} \sum_{n=-\infty}^{\infty} \Phi_{pp}(K_1, k_n) \left| \mathcal{L}^{TE}(x_1, K_1, k_n) \right|^2 |\mathcal{J}|^2 \tag{2}$$

where ρ is the air density, and c_0 represents the speed of sound in the medium. The spectra Φ_{ww} and Φ_{pp} represent the two-dimensional turbulence and pressure power spectral densities, respectively. For the LE case, Φ_{ww} is the incoming turbulence spectrum, while for the TE case, Φ_{pp} is the point spectral density of the pressure field at the trailing-edge [6]. The azimuthal wavenumber k_n corresponds to the gust of mode n, with $k_n = n/r_0$, and the calculations in Eqs. (1) and (2) require summing over discrete modes n from $-\infty$ to ∞. As shown in [6], not all modes are required depending on the reduced frequency kr of interest, as the contribution of modes close to $n = 0$ is more significant.

The term S_0 is the far-field corrected distance given by $S_0^2 = x_1^2 + \beta^2(x_2^2 + x_3^2)$ with $\beta^2 = 1 - M^2$. U represents the mean flow velocity at the

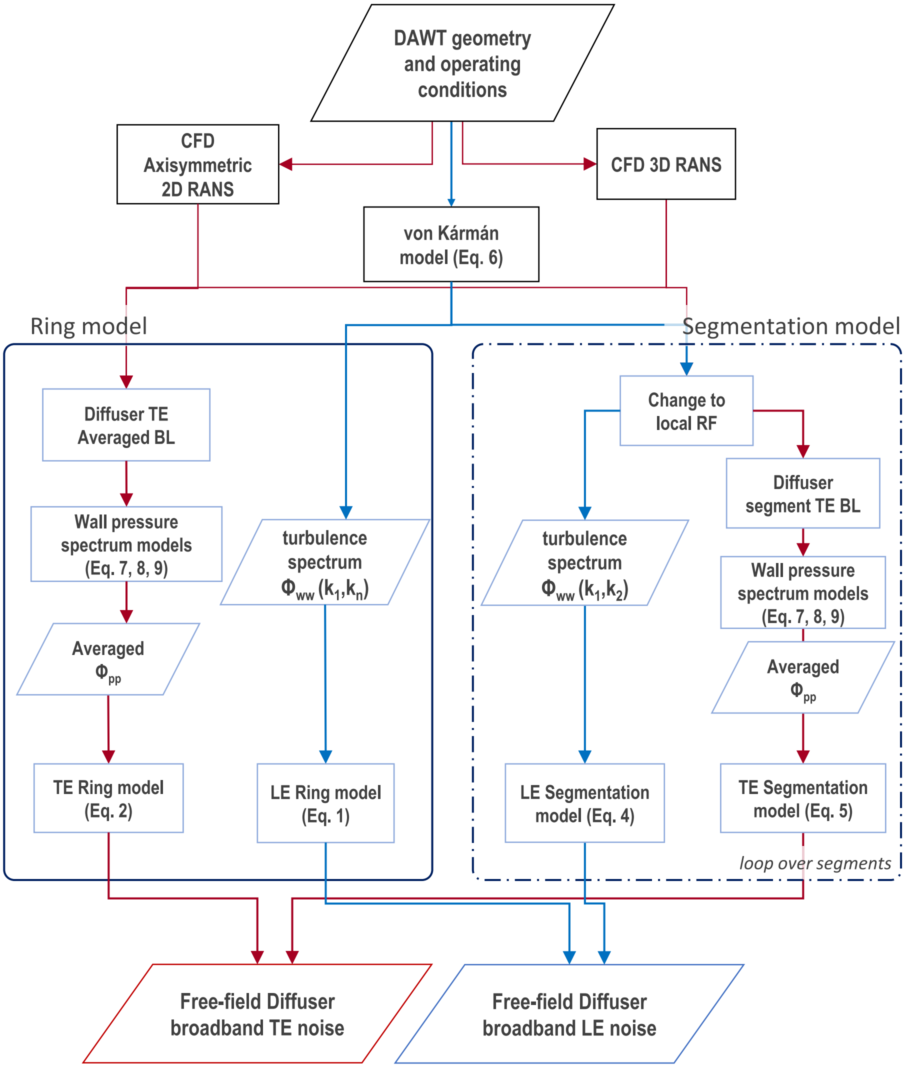

Fig. 2. Simulation flowchart for predicting broadband noise from a diffuser-augmented wind turbine. The process uses two modelling approaches: the Ring model, which considers averaged boundary layer properties, and the Segmentation model, which captures local flow variations along the diffuser surface. Both models use CFD data and wall-pressure spectra to estimate broadband noise from the diffuser's leading-edge and trailing-edge.

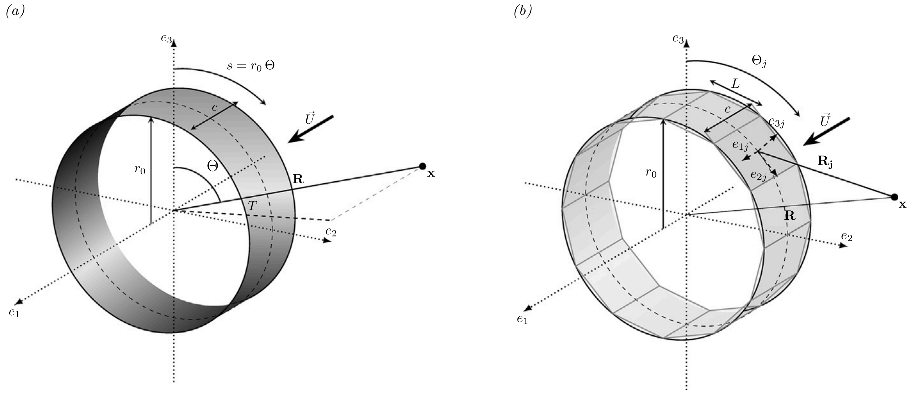

Fig. 3. Schematic showing the two modelling approaches and their associated reference frames. (a) The thin annulus (ring) model assumes axisymmetric loading over a circular geometry and employs a global cylindrical reference frame. (b) The segmentation model [6] divides the circular geometry into discrete flat segments, each with its own local rotating reference frame. The coordinate system is defined by radius r_0, azimuthal angle Θ, arc length $s = r_0\Theta$, and the global basis vectors $\mathbf{e}_1, \mathbf{e}_2, \mathbf{e}_3$. The observer position is denoted by $\mathbf{x}$, the source location by $\mathbf{y}$, the vector $\mathbf{R} = \mathbf{x} - \mathbf{y}$ represents the source–observer separation, and T is the projection of $\mathbf{R}$ in the $\mathbf{e}_1, \mathbf{e}_2$ plane. The axial flow velocity is defined denoted by $\vec{U}$. In the segmentation model, Θ_j and $\mathbf{R}_j$ indicate the angular segment location and the corresponding segment-wise source-observer vector, respectively. The chord length c, segment arc length L, and local basis vectors $\mathbf{e}_1, \mathbf{e}_2, \mathbf{e}_3$, are also shown.

leading-edge, and U_c the convection velocity at the trailing-edge, generally taken as $U_c = 0.7U$ for trailing-edge noise applications [10–12]. $\mathcal{L}^{LE}$ and $\mathcal{L}^{TE}$ are the flat plate LE and TE aeroacoustic transfer functions, and the comprehensive solutions are found in [13,14]. $\mathcal{J}$ denotes an axisymmetric term, written as:

$$|\mathcal{J}|^2 = (2\pi)^2 T^2 \left(\mathbf{J}'_n\left(\frac{kr_0\, T}{S_0}\right)\right)^2, \tag{3}$$

where $\mathbf{J}'_n$ is the derivative of the Bessel function of the first kind, T is the projection of the distance to the observer position vector $\mathbf{R} = \mathbf{x} - \mathbf{y}$ onto the frontal plane defined by coordinates e_2 and e_3 (see Fig. 3) and k is the acoustic wavenumber.

2.1.2. Segmentation model

The segmentation approach, as described in Fig. 2, consists in subdividing the cylindrical geometry into flat-plate airfoils, enabling the use of Amiet's models [15,16] for each segment to predict the total noise as the sum of uncorrelated contributions. Fig. 3(b) demonstrates how the diffuser is discretised into N rectangular segments.

The total broadband noise of a ring with radii r_0 and chord c, is computed using [6]:

$$S_{pp}^{LE}(\mathbf{x},\omega) = \left(\frac{\omega\rho c}{2c_0}\right)^2 \pi U\, \frac{L}{2} \sum_{j=0}^{N} \left(\frac{x_{3j}}{S_{0j}^2}\right)^2 \left|\mathcal{L}^{LE}\left(x_{1j}, K_1, K_{2j}\right)\right|^2 \Phi_{ww}\left(K_1, K_{2j}\right) \tag{4}$$

$$S_{pp}^{TE}(\mathbf{x},\omega) = \left(\frac{\omega c}{4\pi c_0}\right)^2 \frac{L}{2} \sum_{j=0}^{N} \left(\frac{x_{3j}}{S_{0j}^2}\right)^2 \left|\mathcal{L}^{TE}\left(x_{1j}, K_1, K_{2j}\right)\right|^2 \Phi_{pp}(\omega)\, l_y\left(\omega, K_{2j}\right) \tag{5}$$

where K_1 and K_{2j} are the gust's wavenumber in the e_1 (streamwise) and e_2 direction, the segment length L is determined by the number of segments N and the radius r_0 as $L = 2r_0 \sin\frac{\pi}{N}$. The third component of the observer position x_{3j} and distance S_{0j}^2 are computed in the local reference frame of each segment j. For segment j, the observer relative positions and the corrected distance S_{0j} are obtained based on the observer-source relative position $\mathbf{R}$ and plate's angle of attack α with:

$$\begin{aligned}
x_{1j} &= R_1 \cos\alpha + (R_2 \sin\Theta_j + R_3 \cos\Theta_j - r_{\text{seg}}) \sin\alpha - l,\\
x_{2j} &= R_2 \cos\Theta_j - R_3 \sin\Theta_j,\\
x_{3j} &= -R_1 \sin\alpha + (R_2 \sin\Theta_j + R_3 \cos\Theta_j - r_{\text{seg}}) \cos\alpha.
\end{aligned}$$

Accounting for the angle of attack ensures the observer's relative positions and distances are more precisely computed, resulting in a more accurate noise directivity.

2.1.3. Comparison of thin annulus and segmentation models

The thin annulus model and the flat plate segmentation model can both be used to predict the aerodynamic noise of structures like ducts or diffusers. The thin annulus model provides an exact analytical solution for cylindrical geometries, while the segmentation model provides a geometrical approximation that allows the use of the classical Amiet theory. Table 1 summarizes the key differences, assumptions, and computational trade-offs between these two approaches.

A primary limitation of the thin annulus model is the assumption of uniformity in the surface pressure spectrum Φ_{pp} along the angular direction Θ. Although incorporating the azimuthal correlation length l_Θ could address this, no explicit expression for l_Θ has yet been derived. The key advantage of the segmentation approach is that, by subdividing into individual flat plates, it offers greater flexibility to handle complex shapes, such as diffusers with an angle of attack or non-circular flaps found in engineering applications.

The thin annulus model is computationally more efficient, as it requires a single computation involving a discrete summation over individual azimuthal modes, shown in [6] to be sufficient from $n = -50$ to 50 for frequencies of interest to the human hearing. Alternatively, the segmentation model requires a change of reference frame and a computation for each individual segment, resulting in higher computational costs.

Table 1
Comparison of flat plate Segmentation and Thin Annulus Methods.

	Flat plate Segmentation	Thin Annulus
Advantages	- Allows use of diffuser angle of attack - Allows variation of Φ_{pp} across the Θ direction	- Analytical solution for circular geometry - Only 1 computation for whole body
Disadvantages	- Imperfect representation of circular geometry - Requires change of reference frame and noise prediction computation for each flat plate	- Requires uniform Φ_{pp} across the θ direction - Annulus must be strictly cylindrical, ruling out diffuser AoA

2.2. Aerodynamic model

The aerodynamic analysis provides the necessary inputs for the LE and TE noise predictions, specifically the two-dimensional spectra Φ_{ww} and Φ_{pp}. The incoming turbulence spectrum Φ_{ww} is computed using the two-dimensional von Kármán turbulence spectrum model, as detailed in Section 2.2.1, a widely used approach for leading-edge noise prediction studies (e.g., [5,14,17,18]). The point spectral density of the pressure field at the trailing-edge, Φ_{pp}, is modeled using semi-empirical wall pressure spectrum models, which take as input detailed boundary layer parameters at the trailing-edge and have been successfully applied in similar contexts for trailing-edge noise prediction of airfoil, wind turbines and helicopter rotors (e.g., [14,19–22]). Thus, unlike for the LE case, the TE noise modeling requires computational fluid dynamics (CFD) simulations to derive the boundary layer parameters used to compute the wall pressure spectrum, as detailed in Section 2.2.2.

2.2.1. Inflow turbulence spectrum

The incoming turbulence spectrum Φ_{ww} can be obtained using the two-dimensional von Kármán turbulence spectrum model, given by:

$$\Phi_{ww}^{vK}(k_1, k_2) = \frac{4}{9\pi} \frac{u_{rms}^2}{k_e^2} \left(\frac{(k_1/k_e)^2 + (k_2/k_e)^2}{1 + (k_1/k_e)^2 + (k_2/k_e)^2}\right)^{7/3} \tag{6}$$

where u_{rms} represents the root-mean-square velocity, and k_1 and k_2 denote any streamwise and spanwise wavenumbers, respectively. The wavenumber scale k_e, associated with the largest eddies, is defined as:

$$k_e = \frac{\sqrt{\pi}}{\Lambda_f} \frac{\Gamma(5/6)}{\Gamma(1/3)}$$

where Λ_f denotes the characteristic length scale of the turbulence and Γ the gamma function. In the thin annulus model, k_n replaces k_2.

2.2.2. Wall pressure spectrum at the trailing-edge

The wall pressure spectrum (WPS) Φ_{pp} is obtained using semi-empirical models which take as input boundary layer parameters such as boundary layer thickness δ, displacement thickness δ^*, momentum thickness θ, wall shear stress τ_{wall}, boundary layer edge velocity U_e or the pressure gradient $\mathrm{d}p/\mathrm{d}x$ in the streamwise direction. The boundary layer parameters are derived from CFD modeling, as detailed in Section 2.2.4. In this work, the models proposed by Goody [23], Lee [22], and Kamruzzaman [20] were used according to the type of pressure gradient. The diffuser pressure side (PS) will have a favorable pressure gradient (FPG) in the chordwise direction, with the flow being affected only by the diffuser thickness. On the suction side (SS), the rotor wake's presence generates a strong and adverse pressure gradient (APG). The Goody model is a good choice for FPG and will be used

Table 2

Summary of existing studies on ducted configurations, including the focus and their methodology.

Author(s)	Type	Focus	Approach	DonQi
Van and Eng [24]	Experimental	Blade design	–	Yes
Anselmi [25]	Numerical	Aeroacoustics under yaw	LBM + FWH	Yes
Küçükosman [26]	Numerical	Aerodynamics + Acoustics	RANS + Strip theory	Yes
Avallone et al. [27]	Numerical	Aerodynamics + Acoustics	LBM + FWH	Yes
Freire-Guimaraes [4]	Numerical	Aeroacoustics	LBM	Yes
Dighe [28]	Experimental	Diffuser optimization	Actuator Disk	Yes
Bontempo et al. [30]	Numerical	Aerodynamics	RANS	–
Leloudas [29]	Numerical	Diffuser design optimization	Axi RANS + BEM	Yes
Gonçalves et al. [1]	Numerical	Aerodynamics + Acoustics	RANS	Yes
Ahmed et al. [8]	Experimental	Aeroacoustics	–	No
Saleem and Kim [31]	Numerical	Aerodynamics	RANS + MRF	No
Roshan et al. [32]	Numerical + Exp	Aerodynamics	RANS + MRF	No
Noorollahi et al. [33]	Numerical	Aerodynamics	RANS	No
Knight et al. [34]	Numerical	Aerodynamics	RANS + URANS	No

for the pressure side, while the Lee and Kamruzzaman models are more accurate in the presence of APG, as found on the diffuser's suction side.

The Goody model [23] is written:

$$\frac{\Phi_{pp}(\omega)U_e}{\tau_{wall}^2\,\delta} = \frac{3(\omega^*)^2}{[1.0(\omega^*)^0.75+0.5]^{3.7}+[1.1R_T^{-0.57}\,\omega^*]^7} \tag{7}$$

The Lee model [22] is written as:

$$\frac{\Phi_{pp}(\omega)U_e}{\tau_{wall}^2\,\delta^*} = \frac{a\,\max(1,(0.25\beta_c-0.52))\,(\omega^*)^2}{[4.76\,(\omega^*)^{0.75}+d^*]^e+[8.8\,R_T^{-0.57}\,\omega^*]^h} \tag{8}$$

$\omega^* = \omega\,\delta/U_e$, $\beta_c = (\theta/\tau_{wall})/(\mathrm{d}p/\mathrm{d}x)$, $R_T = u_\tau^2\,\delta/(U_e\,\nu)$, the coefficients can be calculated using $a = 2.82\,\Delta^2(6.13\Delta^{-0.75}+d)^e\,[4.2(\Pi/\Delta)+1]$, $d = 4.76(1.4/\Delta)^{0.75}\,[0.375e-1]$ with $d^* = d$, except for $\beta_c < 0.5$ in which case $d^* = \max(1.0, 1.5\,d)$, with $e = 3.7+1.5\beta_c$ and $h = \min(3,(0.0139+3.01043\beta_c))+7$. Finally, $\Pi = 0.8(\beta_c+0.5)^{3/4}$, $\Delta = \delta/\delta^*$.

The Kamruzzaman model [20] is written:

$$\frac{\Phi_{pp}(\omega)U_e}{\tau_{wall}^2\,\delta^*} = \frac{0.45[1.75(\Pi^2\,\beta_c^2)^m+15]\,(\omega^*)^2}{[(\omega^*)^{1.637}+0.27]^{2.47}+[1.15\,R_T'^{-0.2857}\,\omega^*]^7} \tag{9}$$

where R_T' is calculated with δ^* instead of δ, $m = 0.5(H/1.31)^{0.3}$, and the shape factor $H = \delta^*/\theta$. The modified Clauser parameter β_c is obtained through an experimental database curve-fit with the expression:

$$\beta_c = (\,[\,(1-\frac{1}{H})\,\sqrt{2/C_f}+1.7]\,/\,6.1)^2 - 1.81 \tag{10}$$

with C_f defining the friction coefficient and Cole's wake parameter Π obtained using the same expression as in Lee's model, except for $\beta_c \leq -0.5$, in which case $\Pi = 0.227$.

2.2.3. *DonQi wind turbine and literature review*

The wind turbine studied in this work is the commercial DonQi urban wind turbine, a diffuser-augmented horizontal-axis design. This turbine was selected for being the DAWT with the most extensive documentation in the literature.

These operating conditions have been extensively studied in the literature: [24] proposed the blade design optimization and compared the aerodynamic performance experimentally, obtaining $C_p = 0.65$; [25] modeled the diffuser-augmented wind turbine using a high-fidelity simulation and computed the noise using the Ffowcs Williams–Hawkings (FWH) formulation under varying yaw angles; [26] used a 3D RANS approach to model the diffuser-augmented wind turbine and estimated the rotor trailing-edge broadband noise using a strip approach; [27] investigated the influence of the tip-gap size on noise using Lattice-Boltzmann Method (LBM) and FWH; [4] computed the wind turbine power spectral density using LBM and FWH; [28] investigated the diffuser experimentally using an actuator disk made with mesh and proposed design optimizations; finally, [29] modeled the DAWT using an in-house BEM and axisymmetric RANS model, also proposing diffuser design improvements.

Table 2 summarizes the key studies, highlighting their methodologies and main contributions.

2.2.4. *CFD modeling*

CFD modeling was used to extract the boundary layer parameters at the diffuser trailing edge, which are required for modeling the wall pressure fluctuations Φ_{pp} that are used to predict trailing-edge noise. To achieve this, both three-dimensional and two-dimensional axisymmetric approaches were performed using the finite volume solver Simcenter STAR-CCM+ [35]. The 3D approach provides a realistic representation of the rotor and flow conditions around the ducted wind turbine. In contrast, the 2D axisymmetric approach represents an empty duct without actuator disk, resulting in the rotor being neglected in this approach. This simplification is intentionally applied to the diffuser case to investigate the influence of the rotor and to understand the extent to which a simpler, more computationally efficient approach could approximate the results obtained from the more complex 3D model. By comparing these two approaches, we aimed to evaluate the trade-offs between model complexity, computational cost, and the accuracy of the predicted parameters.

2.2.4.1 *Isolated duct and empty diffuser.*

2D axisymmetric simulations were conducted using steady RANS with the turbulence model k-omega SST model incompressible flow. The computational domain represents the middle plane of the duct, with the centerline as the symmetry axis. The domain extends radially to $13r_0$ and has a streamwise extent of $20r_0$. A structured mesh was used, with a target size of 10 mm, surface size of 0.5 mm, and 18 inflation layers near the walls resulting in a total cell count of approximately 77000.

2.2.4.2 *Diffuser-augmented wind turbine.*

A 3D approach was simulated using steady RANS with the k-omega SST turbulence model, following literature best practices [26,30–34]. The computational domain encompasses a 120° sector of azimuthal angle, including the rotor, duct, and hub of the DonQi wind turbine. The domain has a radial extent of $13r_b$ (where r_b is the blade tip radius) and a streamwise extent of $20r_b$, centered on the rotor plane. The turbine's rotation is modeled with a moving reference frame (MRF), with no-slip conditions on all solid surfaces. The polyhedral mesh used in this study is the same as described in [1], consisting of 31.5 million cells. A grid sensitivity study was previously conducted and validated in the [1].

3. Application to isolated duct and DonQi diffuser-augmented wind turbine

The results obtained at each step of the sound prediction chain (Fig. 2) are presented below, divided into two subsections: the cylindrical isolated duct and the diffuser configuration. The isolated duct serves as a validation test case, as its geometry is an intermediate step between the idealized ring used in the theoretical model (Fig. 3), and the more complex design of the DonQi wind turbine's diffuser (Fig. 1), which introduces greater thickness and a non-zero angle of attack. For each configuration, we discuss the aerodynamic results followed by the aeroacoustic analysis.

3.1. Isolated duct

The isolated duct has an average radius of 133.5 mm, with a wall thickness of 12 mm and a length of 175 mm. It features a rounded leading-edge and a blunt trailing-edge. The full geometric parameters are detailed in [8].

3.1.1. Isolated duct test setup

The test setup follows the configuration described in [8], where the CNC-machined aluminum duct was positioned 0.8 m downstream of the nozzle center in the University of Bristol aeroacoustics wind tunnel. This closed-circuit, open-jet facility is specifically designed for experimental aerodynamics and aeroacoustics [36]. The far-field noise measurements for the isolated duct were captured using GRAS 40PL piezoelectric free-field microphones, arranged in a circular array. The microphones were spaced at 5° intervals, covering an angular range from 40° to 140° relative to the duct inlet plane, and positioned 1.75 m from the duct center. To ensure measurement accuracy, each microphone was calibrated using a GRAS 42AA piston phone calibrator. The data acquisition was performed using PXIe-4499 Sound and Vibration modules housed within a PXIe-1062Q chassis from National Instruments. The noise data were captured at a sampling frequency of 2^{16} Hz for a duration of 32 s, providing high-resolution temporal data, essential for detailed analysis of the noise characteristics across varying flow velocities.

3.1.2. Aerodynamic results

The incoming turbulence spectrum Φ_{ww} was computed using the von Kármán model (Eq. (6)), where $u_{rms} = U \times TI\%$ and $\lambda_f = 0.2$. The turbulence intensity (TI) was characterized as 0.1 % based on wind tunnel data from the measurements reported in [36].

Under the studied conditions, the Reynolds number at the duct trailing edge remains in the laminar regime for most of the velocity range. Only at 32 m s^{-1} does the Reynolds number approach approximately $3{\times}10^5$. Given that transitional or turbulent boundary layers are required for trailing-edge noise generation, it can be assumed that, in this case, no substantial trailing-edge noise emission occurs. Consequently, only the leading-edge noise predictions are presented for the isolated duct case, and the CFD results were not considered in this case.

3.1.3. Aeroacoustic results

Fig. 4 shows the comparison of the far-field noise radiation by the thin annulus prediction model and experimental results. The data, acquired at a microphone positioned at $\Theta = 90°$, covers axial incoming velocities from 8 to 32 m s^{-1}. This comparison highlights the model's effectiveness in capturing the leading-edge broadband noise across various flow velocities, evidenced by the close alignment with the experimental data. The noise spectrum shows a strong dependency on flow velocity, with higher velocities resulting in elevated noise levels across the frequency spectrum.

In addition to broadband components, the experimental data reveal distinct peaks that are not captured by the prediction model. These components are associated with vortex shedding at the duct's blunt trailing-edge, which interacts with and excites the internal duct acoustic field, as observed by Ref. [8]. This coupling between vortex shedding and the internal duct acoustics is velocity-dependent, with higher velocities amplifying the response. The underlying mechanisms are explained below.

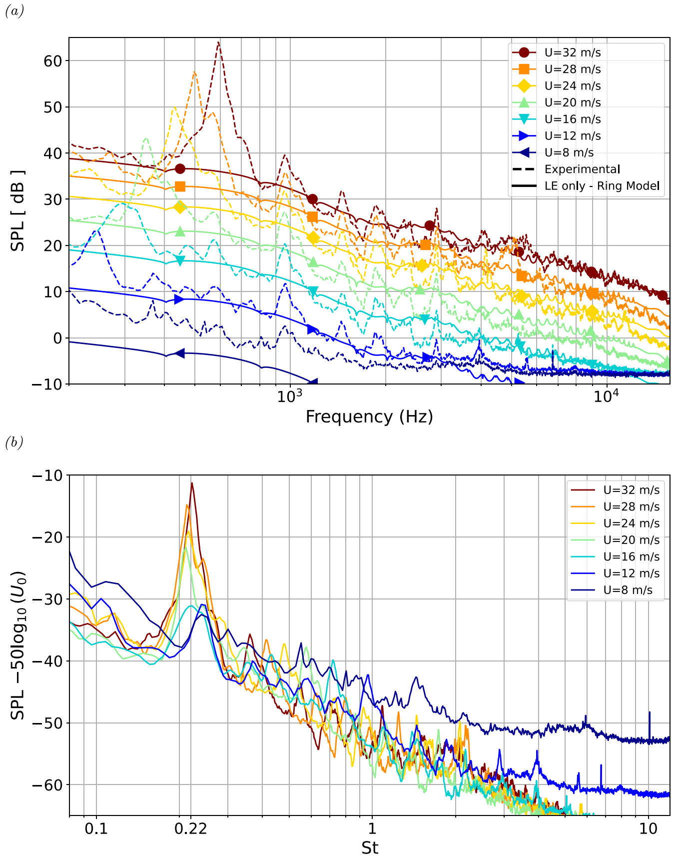

Fig. 4. (a) Sound pressure levels of the isolated duct at $\Theta = 90°$, with model predictions compared against measurements [8] under inflow velocities ranging from 8 to 32 m s^{-1}. and (b) Experimental duct noise measurements at $\Theta = 90°$ with Strouhal number, featuring collapse at 0.22 resulting of blunt trailing edge noise.

To identify the origin of the observed spectral peak features, the spectra were analysed in both dimensional (frequency) and non-dimensional (Strouhal number) forms, as shown in Fig. 4. The non-dimensionalisation was performed using the trailing-edge thickness of the duct as the characteristic length scale and the inflow velocity as the velocity scale. This representation helps distinguish between flow-induced and geometry-induced noise mechanisms as the source of spectral peaks.

When the peaks collapse across different inflow velocities in the Strouhal domain (Fig. 4(b)), they scale with velocity and are therefore indicative of flow-induced mechanisms, such as vortex shedding. This is evident in the dominant low-frequency peaks — for example, the 600 Hz peak at 32 m s^{-1} — which corresponds to a Strouhal number of approximately $St \approx 0.22$. These peaks align across different inflow conditions after rescaling and exhibit a U^5 amplitude scaling, consistent with the fifth-power law for dipole-type noise sources. This provides strong evidence that the low-frequency peak originates from vortex shedding at the blunt trailing-edge of the duct. The corresponding acoustic response of the duct appears as a planar acoustic field, excited by the unsteady aerodynamic forcing from vortex shedding. Specifically, the dominant peak (e.g., 600 Hz at 32 m s^{-1}) lies below the cut-off frequency $f_c \approx 790$ Hz [8], and is therefore associated with planar acoustic propagation within the duct, which then radiates into the far field through open ends of the duct. Therefore, it is confirmed that the

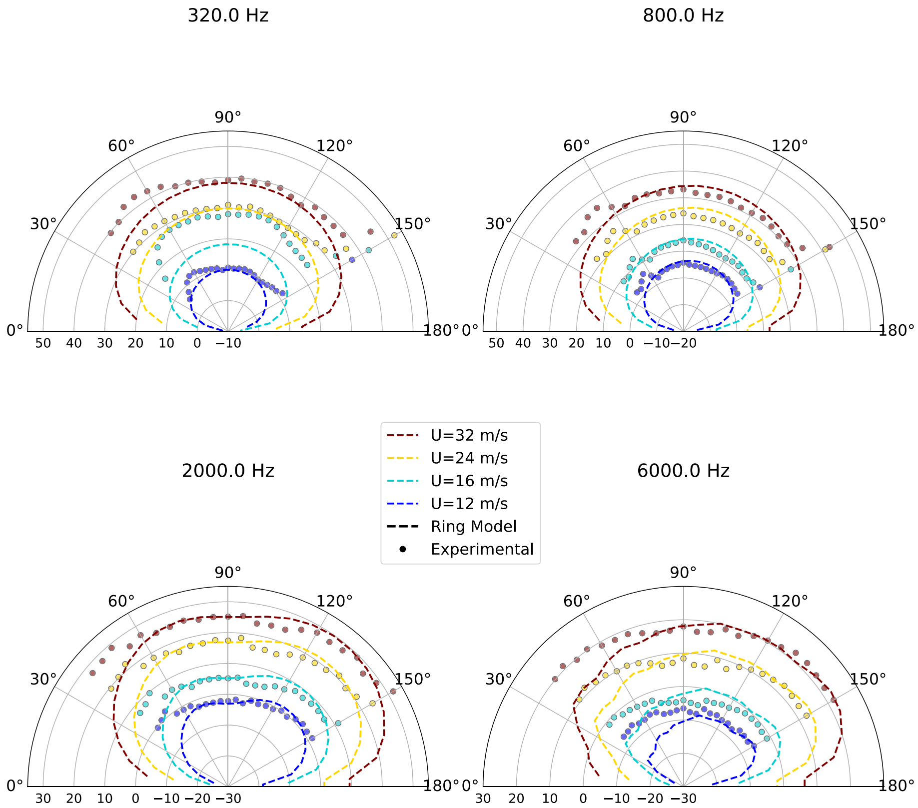

Fig. 5. Sound pressure level (SPL) in dB directivity patterns of the isolated duct at four representative frequencies (320, 800, 2000, and 6000 Hz) under inflow velocities ranging from 12 to 32 m/s. Eas polar plots illustrate the angular distribution of radiated noise, with the flow direction from top (0°) to bottom (180°). Predictions from the thin annulus (Ring) model are compared against experimental data at each frequency.

dominant low-frequency peaks observed in the experimental spectra are attributed to the forced acoustic response of the duct due to vortex shedding from the blunt trailing-edge. This interpretation aligns with the findings reported in [8], which used the same measurement dataset and demonstrated that vortex shedding excites planar duct acoustic waves, leading to distinct low-frequency peaks in the radiated spectrum.

On the other hand, when the peaks do not collapse in the Strouhal domain and instead remain fixed across all velocities (Fig. 4(b)), they are indicative of geometry-induced mechanisms that are independent of the inflow velocity. For example, several peaks around 1000 Hz and its multiples are observed at the same frequencies across all tested velocities. Such behaviour cannot be attributed to flow-induced sources like vortex shedding, suggesting that a different source mechanism is responsible. In this case, the source of these fixed-frequency spectral peak features is attributed to the geometric-induced mechanisms such as, scattering and diffraction. As discussed in [8], the internal acoustic field of a duct can be broadly categorised into two regimes: planar modes dominant below the cut-off frequency ($f_c \approx 790$ Hz), and non-planar modes above it. The observed fixed-frequency peaks around 1000 Hz and multiples fall within the non-planar regime of duct acoustic field and are therefore not a result of flow-induced excitation. Instead, they likely arise from the excitation of higher-order non-planar duct acoustic fields. While the precise identification of the physical origin of these fixed-frequency features is beyond the scope of the present study, they are anticipated to arise from the physics of non-planar duct acoustics, governed predominantly by duct geometry rather than unsteady flow structures.

To gain further insights into the effectiveness of the prediction model in capturing the spatial distribution of broadband noise associated with the duct's trailing-edge, Fig. 5 presents a comparison between model predictions and experimental results. The noise directivity patterns are plotted across low, mid, and high frequencies (320, 800, 2000, and 6000 Hz). The comparison is conducted across various axial incoming velocities (12, 16, 24, 32 m s^{-1}).

The predictions demonstrate good agreement with experimental data across all directions, validating the applicability of our model for broadband noise prediction. At lower frequencies, the directivity of the leading-edge noise has a dipolar shape, similar to what was observed for a ring [6]. At mid to high frequencies, such as 2000 Hz and 6000 Hz, the directivity patterns become more directional towards the downstream direction, resulting from the aeroacoustic transfer function effect at reduced frequencies kc [6].

Despite the overall agreement, some discrepancies are observed. At low frequencies, particularly for the velocity of 16 m s^{-1}, there is a mismatch due to the peaks in the experimental data, as shown in Fig. 4. Additionally, localized spikes in the experimental results at 40° and 150° are likely artifacts arising from the geometry at the ends of the microphone array. These deviations are unrelated to the isolated duct broadband noise.

To provide a more comprehensive and frequency-independent assessment of the noise directivity, Fig. 6 presents the overall sound pressure level (OASPL) directivity plots for both model predictions and experimental results. The OASPL was computed by integrating the spectra over the frequency range from 160 Hz to 6000 Hz, which encompasses the relevant broadband content of the duct's trailing-edge noise. Since the prediction model captures only the broadband component, it was necessary to preprocess the experimental data by filtering out the peaks prior to computing the OASPL to ensure a fair comparison.

The results in Fig. 6 demonstrate strong consistency between the predicted and experimental OASPL directivity patterns, reinforcing the model's ability to capture the spatial characteristics of the broadband trailing-edge noise, regardless of frequency or direction. The overall shape exhibits the expected dipolar distribution. However, discrepancies

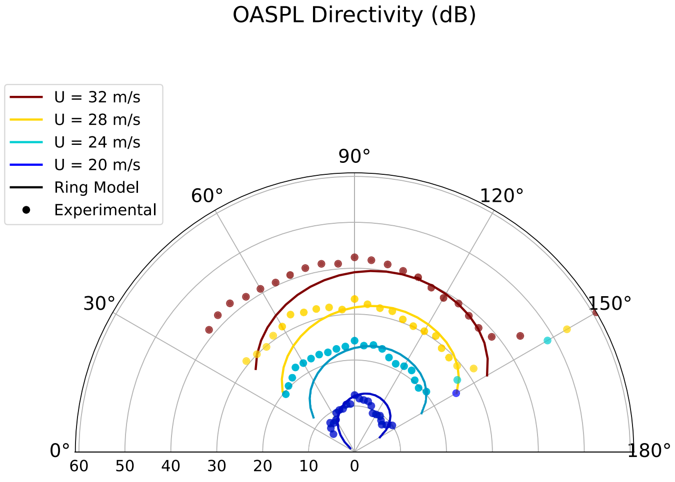

Fig. 6. Overall Sound pressure level (OASPL) directivity patterns of the isolated duct under inflow velocities ranging from 20 to 32 m/s. Predictions from the thin annulus model are compared against the filtered broadband experimental result.

arise around 40° and 150°, where the experimental OASPL is significantly higher than the model predictions and deviates from the dipolar shape. These localized increases were already observed in the frequency-resolved directivity (Fig. 4) and are likely the result of geometric artifacts near the edges of the microphone array, rather than physical noise mechanisms associated with the duct itself.

3.2. *Diffuser-augmented wind turbine*

The turbine used in this study was the DonQi diffuser-augmented wind turbine. The wind turbine has a radius of 0.75 m and a rotational speed of 380 rpm under an inflow of 5 m s^{-1}. Regarding the diffuser, it has diameter equal to $D_{in} = 1.74$ m at the inlet and $D_{out} = 2.0$ m at the outlet, with a cross-section that includes an angle of attack of about 11° and chord length $c = 1.0$ m. Information on the full geometry and operating conditions can be found in [1,27], as well as the detailed CFD model setup and its validation.

3.2.1. *Aerodynamic results*

The boundary layer parameters of the diffuser TE were obtained by extracting data on the diffuser pressure and suction sides. There are 2 different configurations: three-dimensional case and two-dimensional axisymmetric. In the 3D case, the results were processed in two ways: azimuthally averaged and every 2° to capture angular variations. The 2D simulation data is inherently azimuthally averaged, and neglects the rotor as explained in Section 2.2.4.1.

Fig. 7 presents the boundary layer parameters—thickness, momentum thickness, and displacement thickness—obtained from the 3D simulation at the diffuser trailing edge. The pressure side is represented by solid lines, while the suction side is represented with dashed lines.

The results show that the boundary layer parameters are not largely affected by the rotor's tangential position, as the BL thicknesses are mostly constant both on the pressure side and suction side of the diffuser. There is a clear difference in boundary layer thickness, with the pressure side being significantly thicker than the suction side. While this behavior was also noted in the isolated duct case, the difference was less pronounced. The substantially thicker boundary layer on the pressure side of the diffuser is attributed to the high angle of attack of the diffuser cross-section [37] and the rotor wake's influence on the suction side. Downstream of the rotor, the flow is accelerated due to the rotor's tip velocity, which reaches approximately 30 m s^{-1}, exceeding the inflow velocity of 5 m s^{-1}. This results in a higher Reynolds number on the suction side, leading to a thinner boundary layer.

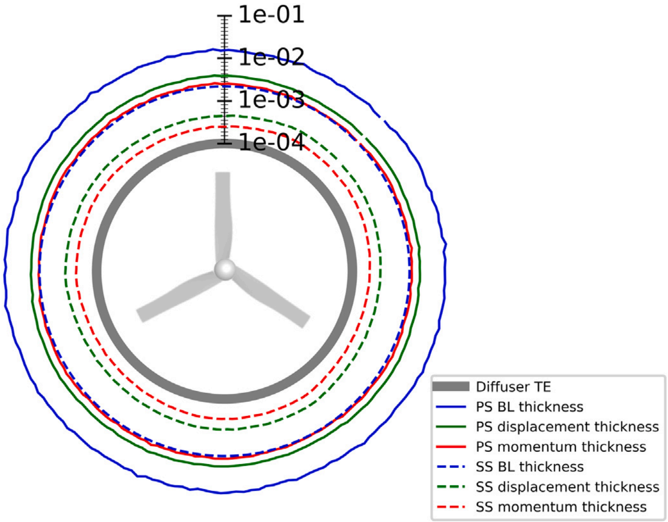

Fig. 7. Circumferential variation of boundary layer thickness parameters along the diffuser trailing edge, extracted from the three-dimensional simulation. Boundary layer thickness, displacement thickness, and momentum thickness are shown for both the pressure side (PS) and suction side (SS), plotted on a logarithmic radial scale in meters.

Table 3 presents the boundary layer parameters used to model the WPS with the 3D and 2D azimuthally averaged approaches, across the pressure side and suction side of the diffuser.

The boundary layer results differ significantly between the 3D and 2D approaches, with values on the PS being up to three times higher in the 3D case. The discrepancies are attributed to the absence of the rotor disk in the 2D approach, which leads to differences in circulation and, consequently, lift. This also explains the variation in pressure gradient and wall shear stress between the two approaches.

Fig. 8 shows the three-dimensional results of the pressure gradient $\mathrm{d}p/\mathrm{d}x$ and wall shear stress τ_{wall} extracted on the pressure and suction sides of the diffuser trailing-edge, plotted as a function of the tangential position along the diffuser trailing-edge. This position is expressed in the rotor-fixed reference frame, where the azimuthal angle remains constant relative to the blades, marked with the vertical dashed lines. Although the diffuser trailing-edge is located approximately 0.8 m downstream of the rotor, the plot highlights the variations induced by rotor passage.

We observe that the pressure gradient on the PS is positive, while on the SS it is negative, validating that the pressure gradient is favorable on the PS and adverse on the SS due to the effect of the rotor slipstream. The wall shear stress is observed to be low and constant on the PS, around 0.08 $\mathrm{N/m^2}$. On the SS, however, the wall shear stress exhibits a sinusoidal pattern with an average amplitude of 0.6 $\mathrm{N/m^2}$.

Fig. 9 presents the wall pressure spectrum's Φ_{pp} on the diffuser TE, obtained using the Goody, Lee and Kamruzzaman WPS models for the three and two-dimensional approaches. As mentioned in Section 2.2.2, the Goody model was used for the prediction of PS, dictated by the FPG, while the Lee and Kamruzzaman models were used for the SS, addressing the APG. For the 3D case, Φ_{pp} was calculated at three angular positions (0°, 30°, and 60°) to evaluate potential variations and assess whether extraction location significantly affects results.

At the PS, the two-dimensional axisymmetric and three-dimensional WPS predictions using the Goody model provide similar results. However, we observe significant differences between the two and three-dimensional approaches at the SS. This disparity arises from the absence of the rotor in the 2D axisymmetric approach, which neglects the rotor-induced flow acceleration and its impact on the suction side. This highlights the rotor's influence on the flow dynamics and the wall pressure spectrum at the trailing edge. Consequently, while the 2D approach

Table 3
Boundary layer parameters of azimuthally averaged approaches.

Case	Side	BL Thickness (mm)	Displacement thickness (mm)	Momentum thickness (mm)	$\mathrm{d}p/\mathrm{d}x$ (Pa m^{-1})	WSS (Pa)	U_e (m s^{-1})
3D	PS	14.98	3.72	2.42	46.86	0.0765	4.75
averaged	SS	2.20	0.49	0.27	-51.14	0.572	11.1
2D only	PS	11.55	1.66	1.17	193.67	0.163	4.9
Diffuser	SS	1.64	0.32	0.13	-16.23	0.018	5.45

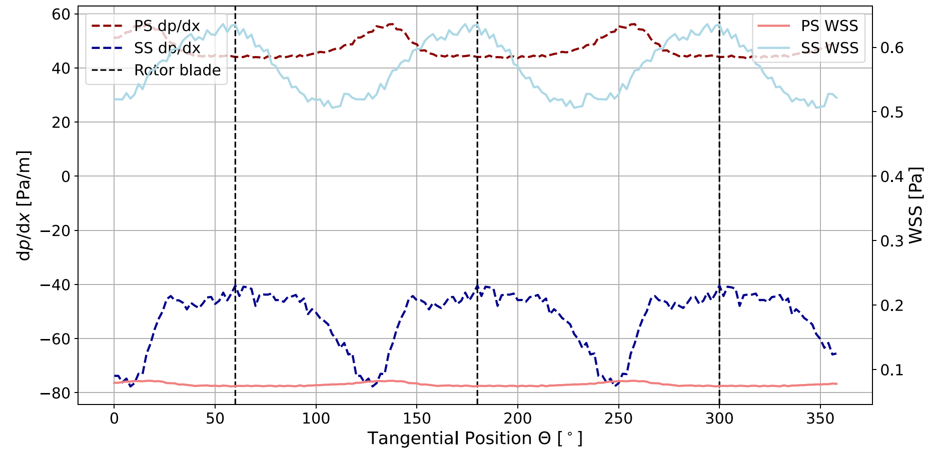

Fig. 8. Circumferential variation of streamwise pressure gradient ($\mathrm{d}p/\mathrm{d}x$) and wall shear stress (WSS) along the diffuser trailing edge, extracted from the three-dimensional case. Results are shown separately for the pressure side (PS) and suction side (SS). Vertical dashed lines indicate the azimuthal positions of the rotor blades.

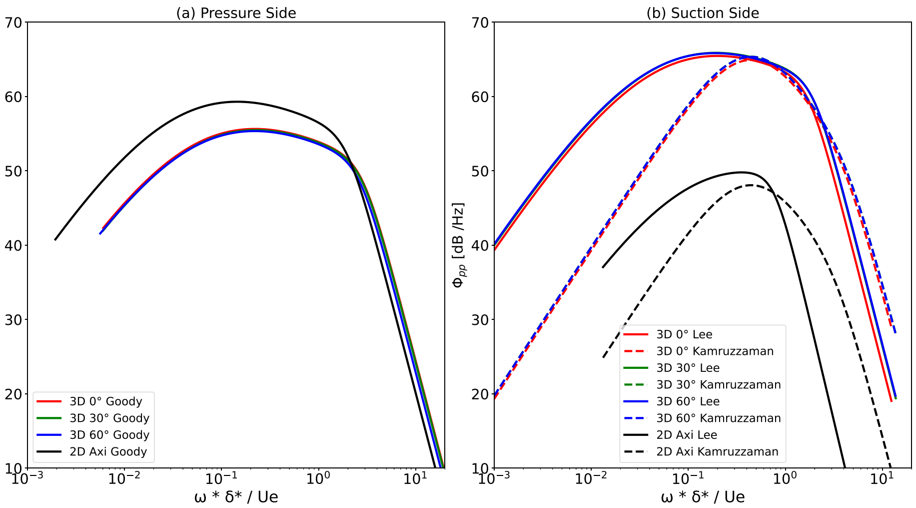

Fig. 9. Prediction of wall pressure spectra at the diffuser trailing edge for the (a) pressure side (PS) and (b) suction side (SS), shown at three circumferential locations (0°, 30°, and 60°) from the three-dimensional case, along with the 2D axisymmetric prediction. Results are compared using the Goody [23], Lee [22], and Kamruzzaman [20] models.

may be suitable for predicting the noise of an empty diffuser, it is unfit to predict the noise of a diffuser-augmented wind turbine. For the 3D approach, the comparison across different angular positions (0°, 30°, and 60°) has a negligible effect on the WPS, despite the wall shear stress and pressure gradient variations observed in Fig. 8.

3.2.2. Aeroacoustic results

The DAWT noise prediction is computed according to Fig. 2 and the results are presented below.

Fig. 10 presents the PSD of the diffuser-augmented wind turbine, including both leading-edge and trailing-edge broadband noise components. The noise predictions are computed using the ring and segmentation models for the 3D case, which incorporates the rotor noise predictions with Kamruzzaman model detailed in [1]. To maintain consistency with the rotor noise predictions, the Kamruzzaman model predictions were applied to the suction side of the diffuser trailing-edge. The 2D axisymmetric case, representing an empty diffuser without rotor, is included to provide comparison. Additionally, the results are compared with LBM FWH predictions from Ref. [4].

The predictions demonstrate good accuracy, particularly at microphones located at 30° and 180° relative to the diffuser axis. At these angles, the predictions deviate by less than 5 dB from the LBM FWH computation. The results show that the dominance of the diffuser TE noise, which surpasses the rotor noise in most directions. The discrepancies observed at 120°, and to a lesser extent at 90°, are likely attributed to physical mechanisms not captured by the current analytical model.

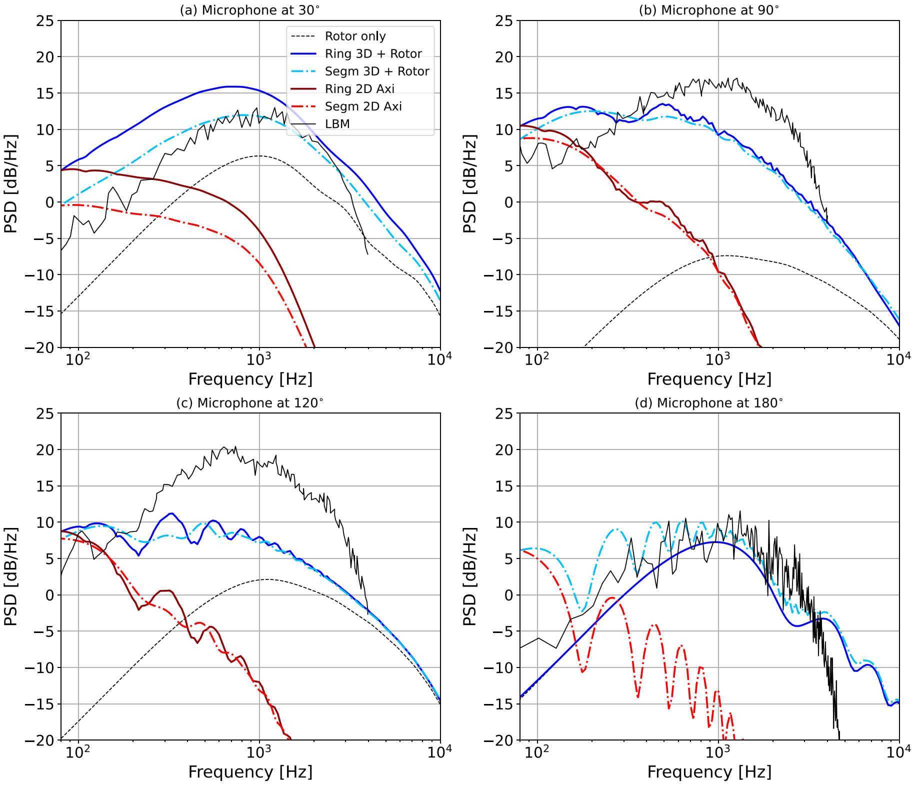

Fig. 10. Broadband noise predictions for the diffuser–rotor configuration, showing contributions from both leading-edge (LE) and trailing-edge (TE) mechanisms. Power spectral density (PSD) is presented at four microphone locations: (a) 30°, (b) 90°, (c) 120°, and (d) 180°. Predictions are obtained using the Ring and Segmentation models with both three-dimensional and axisymmetric inputs. Results are compared against rotor-only data and LBM simulations.

Specifically, our approach does not account for tip vortex noise or its interaction with the diffuser walls, which can result in localized noise generation. Furthermore, the acoustic contribution from the turbulent flow downstream of the rotor is also neglected. These effects, however, are inherently captured in the LBM simulations through the use of permeable Ffowcs Williams–Hawkings surfaces, which integrate acoustic contributions from all relevant flow structures. The additional source mechanisms can be predicted by adopting hybrid approaches such as the model proposed by Ref. [38], which uses RANS data as input to model tip vortex noise.

At 180°, the ring model fails to capture the broadband TE noise of the diffuser, where the predicted noise consists only of rotor noise. This limitation arises due to destructive interference along the rotational axis coming from the directivity of the aeroacoustic transfer function. However, the segmentation approach, incorporating the diffuser's angle of attack, accurately predicts the broadband noise in this direction, particularly at mid and high frequencies. At 30°, the segmentation approach yields significant improvements in the accuracy of the prediction by accounting for the angle of attack, when compared to the ring model.

Finally, the 2D axisymmetric results, representing the noise of an empty diffuser, demonstrate the importance of the rotor interaction in the noise generation process. The absence of the rotor in the 2D case results in significantly reduced TE noise at all frequencies, as a large portion of this component originates from the rotor-induced transition to turbulence and the associated acceleration of the flow, which amplifies the wall pressure spectrum at the diffuser trailing-edge.

Fig. 11 presents the predicted far-field noise directivity of the diffuser-augmented wind turbine using the ring and segmentation models for the diffuser noise prediction. The results are shown at four frequencies: 200 Hz, 600 Hz, 2000 Hz, and 6000 Hz, under the same operating conditions as previously specified, at a distance of 30 m from the rotor. The figure includes the rotor-only noise directivity as a baseline, and the total noise predictions combining the rotor noise with the contributions from the diffuser, for both the ring and segmentation models. Additionally, the individual LE and TE noise components are plotted separately for both modeling approaches.

The directivity predictions in Fig. 11 reveal differences between the ring and segmentation models in certain directions. Due to the underlying assumptions of the ring model, the noise prediction along the axis of the ring (0° and 180°) is zero. In contrast, the segmentation model provides a more accurate representation in these directions by including the effect of the diffuser's angle of attack. Additionally, the ring model tends to overpredict noise levels in the upstream direction, specifically between 10 and 90°. This behavior is consistent with the findings in [6], where the segmentation model results were approximately 2–3 dB lower than the ring model. However, it is important to note that in [6], the angle of attack was set to zero, and the difference was observed uniformly across all frequencies and directions. In the current study, the presence of an angle of attack introduces additional deviations, particularly amplifying the overprediction by the ring model in the upstream direction (with the exception along the axis of the ring).

Under the conditions used in this study, which match those in [27], the leading-edge noise is negligible and is only visible at the lowest frequency on the ring model, making the trailing-edge noise the dominant source in this configuration. However, these conditions do not represent realistic flow conditions as typically found in urban settings, where turbulence intensity is expected to be much higher.

Finally, the rotor noise prediction shows that the rotor is a significant source in certain directions. The rotor and diffuser exhibit distinctive directivity patterns: the rotor, with its dipolar shape, peaks in both the upstream (0°) and downstream (180°) directions. In contrast, the diffuser noise is weak in the downstream direction but, due to the angle

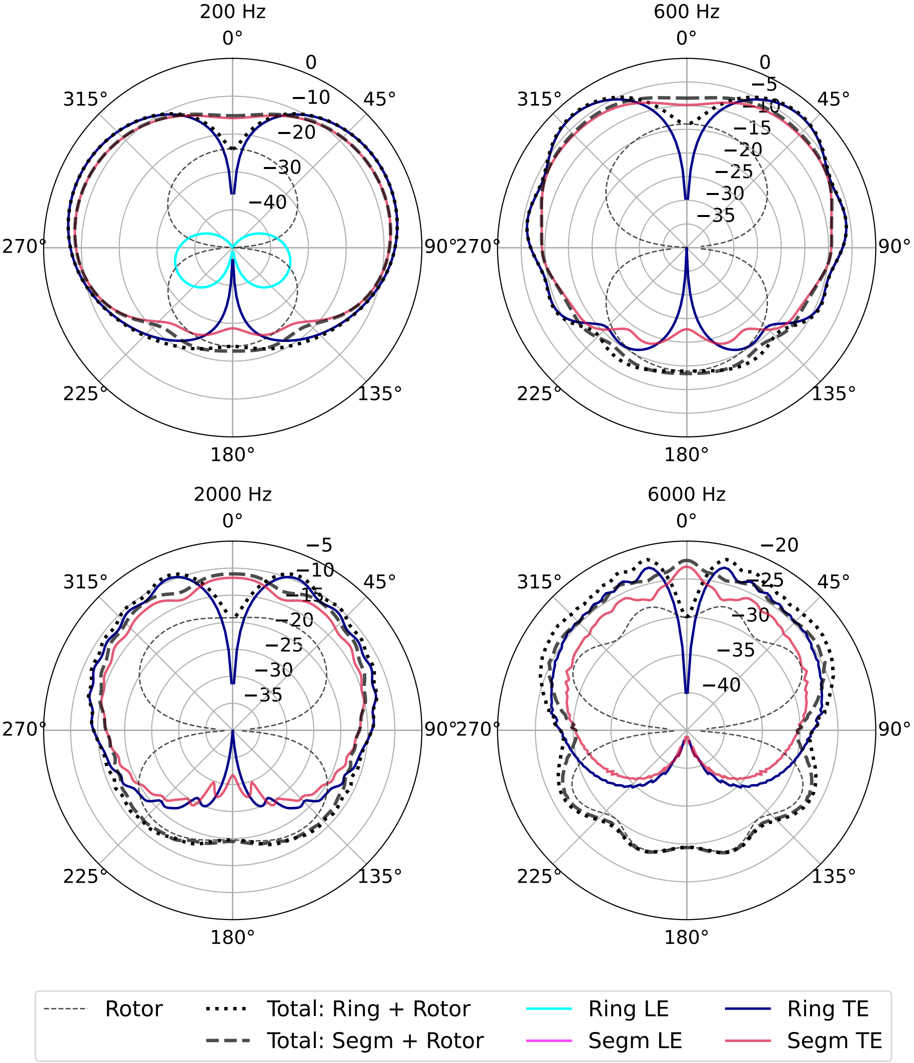

Fig. 11. Noise directivity of the diffuser-augmented wind turbine predicted using the ring and segmentation prediction models at four representative frequencies: 200, 600, 2000, and 6000 Hz. Contributions from leading-edge (LE) and trailing-edge (TE) noise are shown separately for each model, along with the combined rotor–diffuser predictions. Rotor-only noise is included for reference. Flow direction is from top (0°) to bottom (180°).

of attack effect—evident from the difference between the ring and segmentation approaches—it generates a significant noise component in the upstream (0°) direction. At low frequencies, the diffuser noise surpasses the rotor noise, but the rotor plays a more prominent role at mid-to-high frequencies, dominating particularly in the downstream direction. Furthermore, the analysis does not account for the scattering effects of the rotor broadband noise by the diffuser, which could influence the overall noise directivity.

Fig. 12 presents the predicted OASPL directivity of the diffuser-augmented wind turbine at a distance of 30 m from the rotor, including contributions from both leading-edge and trailing-edge noise based on the ring and segmentation models. The results indicate that the diffuser is the dominant noise source in most directions, with the exception of the downstream region, where rotor noise contributions become the significant source. The highest noise levels are observed in the upstream direction, around 30°. As seen before, the two models produce slightly varying results, which do not significantly affect the overall directivity trend. However, the main difference appears in the upstream direction at 0°, where the ring model predicts negligible noise levels, as previously observed.

3.3. Scope and limitations

Some of the observed spectral features – such as low-frequency peaks due to flow-induced mechanisms and fixed-frequency peaks due to geometry-induced mechanisms – are not captured by the present prediction model, which is intentionally formulated to predict broadband noise due to leading-edge turbulence interaction. These simplifications are not limitations, but rather a deliberate design choice that enables the model to reliably capture the global spectral shape across configurations. The goal is not to reproduce every spectral detail, but to offer robust and generalisable predictions for the dominant broadband trends observed across a range of operating conditions.

The scope of this work is restricted to the prediction of broadband noise using an analytical model. As such, several noise-generating mechanisms specific to diffuser-augmented wind turbines were omitted. Notably, the model does not account for tip-vortex noise or its interaction with the diffuser surface, which can be a significant source of localized noise. Capturing such contributions would require either high-fidelity simulations or more complex hybrid models such as the one proposed in [38].

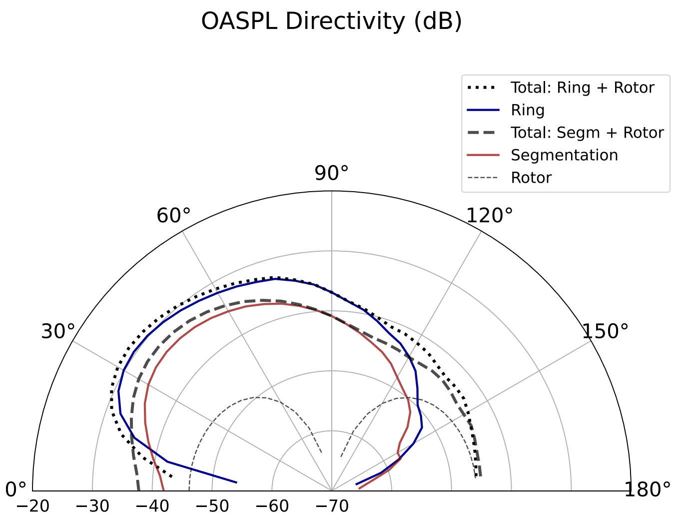

Fig. 12. OASPL (dB) directivity of the diffuser-augmented wind turbine predicted using the ring and segmentation prediction models at 30 m from the rotor. Contributions from leading-edge and trailing-edge noise are included in the ring and segmentation predictions. Flow direction is from top (0°) to bottom (180°).

4. Conclusions

This paper revisits [6]'s proposed aeroacoustic formulations for leading- and trailing-edge noise prediction of hollow cylinders under axial flow, and proposes a noise prediction methodology for ducts and ducted turbine configurations using the mentioned formulations. Both aeroacoustic formulations demonstrate the ability to predict broadband noise effectively. The ring model is well-suited for cylindrical geometries, such as an isolated duct, providing accurate predictions with minimal computational effort. Alternatively, the segmentation approach offers a distinct advantage for geometries with an angle of attack, as demonstrated by the diffuser-augmented wind turbine case.

The results revealed that the isolated duct case predominantly generates leading-edge noise under the specified conditions and geometry, with minimal contribution from trailing-edge noise. In contrast, the diffuser-augmented wind turbine case produces trailing-edge noise, driven by the presence of the rotor and its interaction with the turbulent boundary layer at the diffuser's trailing edge. The comparison showed that the noise from an empty diffuser is significantly lower than that of the diffuser with a rotor, highlighting the critical role of the rotor in amplifying trailing-edge noise by accelerating the flow and triggering turbulence near the diffuser's surface.

The broadband noise directivity reveals distinct rotor and diffuser contributions, each radiating in different directions. The rotor exhibits a dipolar emission pattern with peaking in the axial direction, whereas the diffuser dominates most other directions but contributes little to downstream noise. Consequently, the downstream direction remains dominated by rotor noise, while diffuser noise is the dominant source for a diffuser-augmented wind turbine in all other directions.

CRediT authorship contribution statement

Rui Pedro Gonçalves: Investigation, Data analysis, Writing - review and editing. **Feroz Ahmed:** Data curation. **Christophe Schram:** Writing – review & editing.

Declaration of competing interest

The authors declare the following financial interests/personal relationships which may be considered as potential competing interests: Christophe Schram reports financial support was provided by European Commission. If there are other authors, they declare that they have no known competing financial interests or personal relationships that could have appeared to influence the work reported in this paper.

Acknowledgments

This project has received funding from the European Union's Horizon 2020 research and innovation programme under the Marie Skłodowska-Curie grant agreement No 860101. FA acknowledges the use of the aeroacoustic wind tunnel facility at the University of Bristol for conducting the isolated duct tests.

Data availability

Data will be made available on request.

References

[1] Gonçalves R. Aerodynamics and aeroacoustics of diffuser-augmented wind turbines, Ph.D. thesis, University of Twente, 2025. https://doi.org/10.3990/1.9789036567800
[2] de Vries R, van Arnhem N, Sinnige T, Vos R, Veldhuis LL. Aerodynamic interaction between propellers of a distributed-propulsion system in forward flight. Aerosp Sci Technol 2021;118:107009. https://doi.org/10.1016/j.ast.2021.107009
[3] Hansen MOL, Sørensen NN, Flay RGJ. Effect of placing a diffuser around a wind turbine. Wind Energy 2000;3:207–13. https://doi.org/10.1002/WE.37
[4] Freire-Guimaraes JM, Avallone F, Ragni D. Noise source identification on a diffuser-augmented wind turbine using Ffowcs Williams–Hawkings analogy. In: Book of proceedings 18th EAWE PhD seminar; 2022. p. 133–6. https://phd2022.eawe.eu/program/book-of-abstracts/
[5] Roger M. On broadband jet–ring interaction noise and aerofoil turbulence-interaction noise predictions. J Fluid Mech 2010;653:337–64. https://doi.org/10.1017/S0022112010000285
[6] Gonçalves RP, Bresciani AP, Schram C. Extension of Amiet's theory to circular geometry. J Acoust Soc Am 2025.
[7] Bridges J, Envia E, Huff D. Recent developments in U.S. Engine noise reduction research. 2001.
[8] Ahmed F, Zaman I, Rezgui D, Azarpeyvand M. Aeroacoustics of a ducted fan ingesting an adverse pressure gradient boundary layer. J Fluid Mech 2024;985:R1. https://doi.org/10.1017/jfm.2024.134
[9] Malgoezar AM, Vieira A, Snellen M, Simons DG, Veldhuis LL. Experimental characterization of noise radiation from a ducted propeller of an unmanned aerial vehicle. Int J Aeroacoust 2019;18:372–91. https://doi.org/10.1177/1475472X19852952
[10] Botero L, dos Santos FL, Venner C, de Santana LD. The increase of the airfoil trailing edge noise and unsteady surface pressure due to high inflow turbulence. In: AIAA aviation 2021 forum; Reston, Virginia: American Institute of Aeronautics and Astronautics; 2021. https://doi.org/10.2514/6.2021-2234
[11] Howe M. A review of the theory of trailing edge noise. J Sound Vib 1978;61:437–65. https://doi.org/10.1016/0022-460X(78)90391-7
[12] Stalnov O, Chaitanya P, Joseph PF. Towards a non-empirical trailing edge noise prediction model. J Sound Vib 2016;372:50–68. https://doi.org/10.1016/j.jsv.2015.10.011
[13] Roger M, Moreau S. Back-scattering correction and further extensions of Amiet's trailing-edge noise model. Part 1: Theory. J Sound Vib 2005;286:477–506. https://doi.org/10.1016/j.jsv.2004.10.054
[14] Bresciani AP, Le Bras S, de Santana LD. Generalization of Amiet's theory for small reduced-frequency and nearly-critical gusts. J Sound Vib 2022;524:116742. https://doi.org/10.1016/j.jsv.2021.116742
[15] Amiet RK. Acoustic radiation from an airfoil in a turbulent stream. J Sound Vib 1975;41:407–20. https://doi.org/10.1016/S0022-460X(75)80105-2
[16] Amiet RK. Noise due to turbulent flow past a trailing edge. J Sound Vib 1976;47:387–93. https://doi.org/10.1016/0022-460X(76)90948-2
[17] Paterson RW, Amiet RK. Acoustic radiation and surface pressure characteristics of an airfoil due to incident turbulence, Technical Report, Tech. Rep. CR 2733. NASA, 1976.
[18] Botero-Bolívar L, dos Santos FL, Venner CH, de Santana LD. Experimental and predicted leading- and trailing-edge noise of symmetric airfoils under zero mean-loading. Appl Acoust 2023;212:109579. https://doi.org/10.1016/j.apacoust.2023.109579
[19] dos Santos FL, Botero-Bolívar L, Venner CH, de Santana LD. Wall-pressure spectra, spanwise correlation, and far-field noise measurements of a NACA 0008 airfoil under uniform and turbulent inflows. Appl Acoust 2023;211:109546. https://doi.org/10.1016/j.apacoust.2023.109546
[20] Kamruzzaman M, Bekiropoulos D, Lutz T, Würz W, Krämer E. A semi-empirical surface pressure spectrum model for airfoil trailing-edge noise prediction. Int J Aeroacoust 2015;14:833–82. https://doi.org/10.1260/1475-472X.14.5-6.833
[21] Rozenberg Y, Roger M, Moreau S. Fan blade trailing-edge noise prediction using RANS simulations. J Acoust Soc Am 2008;123:3688. https://doi.org/10.1121/1.2935064
[22] Lee S, Shum JG. Prediction of airfoil trailing-edge noise using empirical wall-pressure spectrum models. Aiaa J 2019;57:888–97. https://doi.org/10.2514/1.J057787

[23] Goody M. Empirical spectral model of surface pressure fluctuations. Aiaa J 2004;42:1788–94. https://doi.org/10.2514/1.9433

[24] Van FA, Eng DB. An improved rotor design for a diffuser augmented wind turbine: improvement of the DonQi urban windmill. 2011. https://repository.tudelft.nl/islandora/object/uuid%3Ac58191fd-dad9-4aa7-8492-113c3b19b7fa

[25] Anselmi L. Computational analysis of ducted wind turbines noise. 2017. https://repository.tudelft.nl/islandora/object/uuid%3Afb9c7edd-8011-428e-bd77-f0e80e7bb60f

[26] Küçükosman C. Semi-analytical approaches for the prediction of the noise produced by ducted wind turbines, Ph.D. thesis, Delft University of Technology, 2019. https://doi.org/10.4233/uuid:b749675c-edb1-4355-ba09-bf46278077d0

[27] Avallone F, Ragni D, Casalino D. On the effect of the tip-clearance ratio on the aeroacoustics of a diffuser-augmented wind turbine. Renew Energy 2020;152:1317–27. https://doi.org/10.1016/J.RENENE.2020.01.064

[28] Dighe V. Ducted wind turbines revisited: a computational study, Ph.D. thesis, Delft University of Technology, 2020. https://doi.org/10.4233/uuid:56111690-faa8-4d98-9aba-d4a43fd5e160

[29] Leloudas SN. Design and optimization of diffuser-augmented wind turbines, Doctoral dissertation, School of Production Engineering and Management, Chania, Greece: Technical University of Crete; 2024.

[30] Bontempo R, Marzo EMD, Manna M. Diffuser augmented wind turbines: a critical analysis of the design practice based on the ducting of an existing open rotor. J Wind Eng Ind Aerodyn 2023;238:105428. https://doi.org/10.1016/J.JWEIA.2023.105428

[31] Saleem A, Kim MH. Effect of rotor tip clearance on the aerodynamic performance of an aerofoil-based ducted wind turbine. Energy Convers Manag 2019;201:112186. https://doi.org/10.1016/J.ENCONMAN.2019.112186

[32] Roshan SZ, Alimirzazadeh S, Rad M. RANS simulations of the stepped duct effect on the performance of ducted wind turbine. J Wind Eng Ind Aerodyn 2015;145:270–9. https://doi.org/10.1016/j.jweia.2015.07.010

[33] Noorollahi Y, Ghanbari S, Tahani M. Numerical analysis of a small ducted wind turbine for performance improvement. 2019;39:290–307. https://doi.org/10.1080/14786451.2019.1685520

[34] Knight B, Freda R, Young YL, Maki K. Coupling numerical methods and analytical models for ducted turbines to evaluate designs. J Mar Sci Eng 2018;6:43. https://doi.org/10.3390/JMSE6020043

[35] Siemens Digital Industries Software. Simcenter STAR-CCM+ user guide (version 2210), Siemens. 2022.

[36] Mayer YD, Jawahar HK, Szőke M, Ali SAS, Azarpeyvand M. Design and performance of an aeroacoustic wind tunnel facility at the University of Bristol. Appl Acoust 2019;155:358–70. https://doi.org/10.1016/j.apacoust.2019.06.005

[37] Goodman S, Gunasekaran S, Altman A, Medina A. On the near wake turbulent flow properties of the SD7003 airfoil. In: AIAA Scitech 2019 forum; American Institute of Aeronautics and Astronautics; 2019. https://doi.org/10.2514/6.2019-0073

[38] Tormen D, Giannattasio P, Zanon A, Gennaro MD, Kühnelt H. Semi-analytical tip vortex model for fast prediction of contrarotating open rotor noise. Aiaa J 2021;59:1629–44. https://doi.org/10.2514/1.J059314